The 2025 World Congress on
Advances in Structural Engineering and Mechanics (ASEM25)
BEXCO, Busan, Korea, August 11-14, 2025

Seismic Response Analysis Methods for Slender Bridge Piers under Bidirectional Earthquake Excitation

Yan Lu, *Hongjing Li, Guangjun Sun and Xiaopeng Yang
Engineering Mechanics Institute, Nanjing Tech University, Nanjing 211816, China.
Yan Lu

Email: lu_yan@njtech.edu.cn

*Hongjing Li

Corresponding author Email: hjing@njtech.edu.cn

Abstract:
Slender bridge piers are critical components of a bridge's seismic system; their significant flexibility and mass inertia amplify gravity-induced second-order effects and higher-mode contributions. However, engineering practice often simplifies the *P*–Δ effect to a single-degree-of-freedom amplification factor, which fails to fully capture the structural safety. To address this limitation, the present study discusses two high-precision, discretization-based dynamic analysis methods: the Differential Quadrature Method (DQM) and the Quadrature Element Method (QEM). Applied to various pier configurations, both methods can stably and efficiently capture dynamic responses under bidirectional seismic excitation, accurately revealing the influence of gravity loads and vertical ground motions on the lateral vibration characteristics of the piers, while comprehensively accounting for *P*–Δ effects throughout the full dynamic analysis. Numerical comparisons demonstrate that by simultaneously considering lateral and axial dynamic loads, these methods significantly improve seismic response prediction accuracy, providing a robust numerical tool for the seismic design and safety evaluation of tall bridge piers.

Keywords:
P–Δ effect; differential quadrature method; bidirectional earthquake excitation; quadrature element method; tall pier.

1. Introduction

Many bridges seismic systems worldwide incorporate tall piers. Owing to their increased flexibility, higher ratio of self‐weight to tributary superstructure mass, and the coupled influence of axial loads on dynamic properties, the seismic response of tall piers differs markedly from that of short piers. The enhanced flexibility of tall piers lengthens their fundamental horizontal period, thereby reducing the seismic acceleration demand in accordance with response spectrum theory. Under such conditions, the implementation of base isolation or the design for high ductility is often neither economically justified nor structurally necessary. Consequently, tall piers are typically designed to remain elastic under seismic loading to ensure performance within the elastic range [1-4].

In most national bridge seismic design codes, the single-degree-of-freedom (SDOF) approach is widely adopted as a primary tool for seismic response analysis, particularly in cases where structural dynamics are dominated by the fundamental mode. Due to its computational simplicity and engineering

practicality, this method plays a central role in routine design applications. However, to ensure its applicability and reliability, design codes generally prescribe specific conditions under which the SDOF assumption is valid—primarily governed by the mass ratio between the pier and the tributary superstructure, as well as the modal characteristics of the system. For instance, Section 4.2.2 of Eurocode 8 – Part 2 explicitly states that the fundamental mode method may only be applied when the pier mass does not exceed 20% of the supported superstructure mass [5]. Similarly, Section 4.7.4.3.2 of the AASHTO LRFD Bridge Design Specifications further defines the "Single-Mode Spectral Method" and the "Uniform Load Method" as simplified equivalent static procedures applicable to bridges where the first mode dominates and mass distribution is relatively regular [6]. In China, Specifications for Seismic Design of Highway Bridges (JTG/T 2231-01—2020) introduces geometric criteria to assess the validity of simplified models. Specifically, it requires that P–Δ geometric nonlinearity be considered when the ratio of the pier height to the shorter side of its rectangular cross-section exceeds 8, or when the height-to-diameter ratio of a circular pier exceeds 6 [7]. This provision, which directly references the seismic design criteria from CALTRANS, indirectly underscores the limitation of SDOF models in capturing the response of increasingly flexible systems where higher-mode effects become significant. In tall pier bridges, the mass of the pier typically exceeds that of the tributary superstructure, and the structural flexibility is considerably greater. Under such conditions, higher-mode contributions to seismic response become non-negligible. Continued reliance on SDOF models may thus lead to underestimation of structural demands. Accurate modeling of the pier geometry and inertia distribution, along with the use of multi-mode or time-history analysis methods, is essential to fully capture the dynamic behavior and to ensure analytical fidelity and seismic safety [8-10].

Recent shake-table and hybrid-model tests have demonstrated that higher-order modes play a pivotal role in the seismic response of tall bridge piers: they not only induce pronounced bending‐moment peaks at mid-height but can also precipitate additional plastic hinges under intense ground motions (e.g., PGA > 0.8 g) [11-13]. Concurrently, axial loads exert a dual influence on pier dynamics—modifying natural frequencies and modal participation factors even within the elastic range, and markedly amplifying second-order (P–Δ) effects as the structure approaches its collapse state. Although current practice often resorts to bending-moment amplification factors—derived from SDOF hysteretic models as per EC8 (§5.4), AASHTO LRFD (§4.5.3.2.2b)—these simplifications frequently fail to replicate the complex dynamic behavior of tall piers with sufficient fidelity.

To overcome these limitations, Tubaldi [14] proposed a nondimensional analytical model that simultaneously accounts for axial loads and higher-mode effects; however, this model cannot accommodate time-varying axial loads induced by vertical seismic excitation. Building on this, the present study primarily introduces two high-precision methods for analyzing the dynamic P–Δ effect in tall bridge piers. These methods are based on the governing differential equations of a cantilever beam subjected to bidirectional coupled loads and are solved using the Differential Quadrature Method (DQM) and the Weak-Form Quadrature Element Method (QEM), respectively. Numerical analyses of various practical pier configurations, benchmarked against the analytical solutions presented in [14], demonstrate the accuracy and broader applicability of the proposed approaches.

2. Analytical Model and Formulation

As shown in Fig. 1, the slender bridge pier is modeled as a linearly elastic Euler–Bernoulli cantilever beam, with flexural stiffness $EI(y)$ and axial stiffness $EA(y)$, mass per unit length $m(y)$, and a concentrated tip mass M_T at the top.

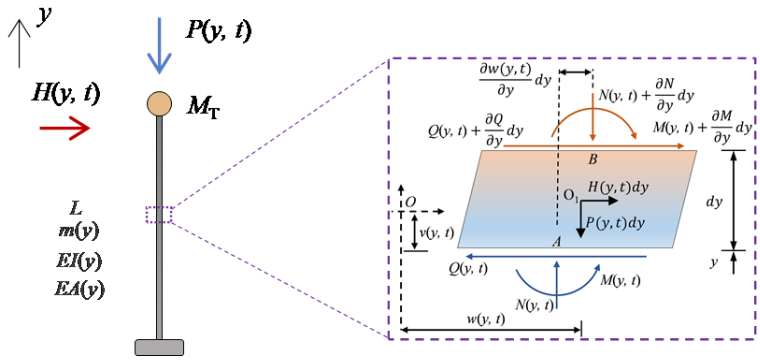

Fig.1. Geometry of the problem and pier model.

In the structural model of Fig. 1, the lateral load H and the axial load P may vary arbitrarily as functions of t and y. Considering an infinitesimal element of length dy at coordinate y, its free-body is shown in Fig. 1. Applying Newton's second law in the horizontal and vertical directions then yields the element's differential equations of motion:

Horizon direction:

$$m(y)\frac{\partial^2 w}{\partial t^2}+\frac{\partial}{\partial y^2}\left[EI(y)\frac{\partial^2 w}{\partial y^2}\right]+\frac{\partial}{\partial y}\left(N\frac{\partial w}{\partial y}\right)=H(y,t) \tag{1}$$

Vertical direction:

$$m(y)\frac{\partial^2 v}{\partial t^2}-\frac{\partial}{\partial y}\left[EA\frac{\partial v}{\partial y}\right]=P(y,t) \tag{2}$$

Where the $w(y, t)$ denotes the lateral displacement (positive to the right), and $v(y, t)$ denotes the vertical displacement (positive downward). $H(y, t)$ and $P(y, t)$ are the lateral and axial distributed loads acting on the structure, respectively. $N(y, t)$ denotes the axial force response.

The time-varying axial force $N(y, t)$ can be determined based on Hooke's law, namely

$$N(y,t)=EA(y)\frac{\partial v(y,t)}{\partial y} \tag{3}$$

By analyzing Equations (1), (2), and (3), it can be seen that the P–Δ effect constitutes a geometrically nonlinear problem. Eq. (2) can be solved independently to obtain the vertical displacement $v(y, t)$, which is then substituted into Eq. (3) to calculate the axial force, followed by substitution into Eq. (1) to solve for the lateral displacement $w(y, t)$. Solving these two equations allows for obtaining a high-precision dynamic P–Δ solution of the structure.

2.1 Methodology Based on the DQM

When applying the Differential Quadrature Method (DQM) to Equations (1) and (2), we first discretize these strong-form partial differential equations and then employ the DQ principle to establish the mapping relationships between the displacement to be solved and its derivatives, thereby obtaining the DQ-formulated differential equations. The detailed procedure has been thoroughly described in our prior work [15]. This paper focuses solely on presenting the fundamental concepts and workflow of the DQM to clarify the methodology.

By discretizing Eq. (1), it can be equivalently expressed in the following form:

$$m\ddot{u} + \frac{1}{L^4}(EI(\xi)\cdot w^{(4)} + 2EI'\cdot w''' + EI''\cdot w'' + L^2\cdot N\cdot w'' + L^2\cdot N'\cdot w') = H(\xi,t) \tag{4}$$

Employing the DQ principle to establish the mapping relationship and expressed in matrix form, it can be written as:

$$\boldsymbol{M\ddot{w}} + \frac{1}{L^4}\left(\boldsymbol{EI}\cdot\boldsymbol{A}^{(4)} + 2\boldsymbol{EI'}\cdot\boldsymbol{A}^{(3)} + (\boldsymbol{EI''} + L^2\cdot\boldsymbol{N})\cdot\boldsymbol{A}^{(2)} + L^2\cdot\boldsymbol{N'}\cdot\boldsymbol{A}^{(1)}\right)\boldsymbol{w}_j = \boldsymbol{H} \tag{5}$$

Here, matrix **A** denotes the weighting-coefficient matrix of the DQ method. The static axial force $N(y)$ is obtained from the following Eq. (6), while the time-dependent axial force $N(y, t)$ is computed by applying DQ discretization to Eq. (2) and incorporated at each time step during the time integration.

$$N(y) = \int_y^L m(\xi)g d\xi \tag{6}$$

Eq. (5) can be solved using the Newmark-β time integration method. When the right-hand side is set to zero, the structure's natural dynamic properties are obtained; with seismic excitation applied, its dynamic response can be evaluated. However, directly introducing the concentrated top mass M_T into the global mass matrix in the DQ framework leads to a discontinuity that may cause numerical instability or divergence. To address this issue, an interpolation-based method is adopted to construct a smooth mass distribution function $m(y)$ that incorporates M_T continuously, improving numerical stability and ensuring reliable dynamic response results [15].

2.2 Methodology Based on the QEM

2.2.1 Formulation of the Hermite-type quadrature element

Compared with the DQM, the QEM offers greater convenience in handling systems with discontinuous masses, as it integrates the advantages of both DQ and finite element concepts. By applying the weak form to the governing dynamic equations in strong form, expressions for the element kinetic and strain energy can be derived.

$$T = \frac{1}{2}\int_0^L \rho A\left(\frac{\partial w}{\partial t}\right)^2 dx \tag{7}$$

$$U = \frac{1}{2}\int_0^L EI\left(\frac{\partial^2 w}{\partial x^2}\right)^2 dx \tag{8}$$

Meanwhile, the work done by the axial force N and the transverse load H can be expressed respectively as:

$$W_n = \frac{1}{2}\int_0^L N(x)\left(\frac{\partial w}{\partial x}\right)^2 dx \tag{9}$$

$$W_h = \boldsymbol{H}^T\boldsymbol{w} = \int_0^L H(x)\,w(x)dx \tag{10}$$

A beam element is assumed to consist of N_n nodes, with one end node located at each boundary and the remaining nodes treated as internal nodes. Since axial deformation is neglected, each internal node possesses a single transverse degree of freedom, while each end node is assigned two degrees of freedom: transverse displacement and sectional rotation. The quadrature element model of the beam is illustrated in Fig. 2.

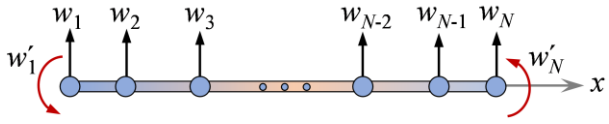

Fig.2. N_n-node quadrature Euler-Bernoulli beam element.

The displacement field of the above N_n-node beam element can be assumed according to the Hermite-type quadrature element formulation.

$$w(x,t)=\sum_{i=1}^{N}\varphi_i(x)w(x_i,t)+\psi_1(x)w^{(1)}(x_1,t)+\psi_N(x)w^{(1)}(x_N,t)=\sum_{i=1}^{N+2}H_i(x)\bar{w}_i(t) \tag{11}$$

where, $\bar{w}_j$=w_j (j =1, 2, ..., N), $\bar{w}_{N+1}$ =$w_1^{(1)}$, $\bar{w}_{N+2}$ =$w_N^{(1)}$, H_i denotes the Hermite interpolation functions, which are defined as follows:

$$H_i(x)=\varphi_i(x)=\begin{cases}\dfrac{1}{(x_i-x_1)(x_i-x_N)}l_i(x)(x-x_N)(x-x_1) & (i=2,3,\dots,N-1)\\ \dfrac{1}{x_i-x_{N-i+1}}l_i(x)(x-x_{N-i+1})-\left[a_{ii}+\dfrac{1}{x_i-x_{N-i+1}}\right]\psi_i(x) & (i=1,N)\end{cases} \tag{12}$$

$$\begin{cases}H_{N+1}(x)=\psi_1(x)=\dfrac{1}{(x_1-x_N)}l_1(x)(x-x_1)(x-x_N)\\ H_{N+1}(x)=\psi_N(x)=\dfrac{1}{(x_N-x_1)}l_N(x)(x-x_N)(x-x_1)\end{cases} \tag{13}$$

where, $l_i(x)$ is the Lagrange interpolation polynomial, and a_{ii} denotes the weighting coefficient of the first derivative of the Lagrange polynomial, which are calculated according to the following formula.

$$l_i(x)=\frac{(x-x_1)(x-x_2)\dots(x-x_{i-1})(x-x_{i+1})\dots(x-x_N)}{(x_i-x_1)(x_i-x_2)\dots(x_i-x_{i-1})(x_i-x_{i+1})\dots(x_i-x_N)}=\prod_{\substack{k=1\\k\neq i}}^{N}\frac{x-x_k}{x_i-x_k} \tag{14}$$

$$a_{ij}=\left.\frac{\partial l_j(x)}{\partial x}\right|_{x=x_i}=\begin{cases}\displaystyle\prod_{\substack{k=1\\k\neq i,j}}^{N}(x_i-x_k)\Big/\prod_{\substack{k=1\\k\neq i,j}}^{N}(x_j-x_k) & (i\neq j)\\ \displaystyle\sum_{\substack{k=1\\k\neq i}}^{N}\frac{1}{x_i-x_k} & (i=j)\end{cases} \tag{15}$$

To obtain the diagonal mass matrix of the element [16], the displacement field can be interpolated using Lagrange shape functions, which allows the integral formulation of the mass matrix to be constructed.

$$w(x,t)=\sum_{i=1}^{N}l_i(x)w(x_i,t)=\sum_{i=1}^{N}l_i(x)w_i(t) \tag{16}$$

By substituting the Lagrange-based displacement field into Eq. (7), and further substituting Eq. (11) into Equations (8) and (9), the resulting formulations can be expressed using the dimensionless nodal coordinates ξ_i(i =1, 2, …, N), where ξ=(2x-L)/L, leading to:

$$T=\frac{1}{2}\int_{-1}^{1}\frac{m(\xi)L}{2}\left(\sum_{i=1}^{N}l_i(\xi)\,\dot{w}_i(t)\right)^2 d\xi=\frac{1}{2}\dot{\boldsymbol{w}}^{\boldsymbol{T}}\boldsymbol{m}\dot{\boldsymbol{w}} \tag{17}$$

$$U=\frac{1}{2}\int_{-1}^{1}\left(\frac{8EI(\xi)}{L^3}\right)\left(\sum_{i=1}^{N+2}\frac{d^2H_i(\xi)}{d\xi^2}\bar{w}_i(t)\right)^2 d\xi=\frac{1}{2}\bar{\boldsymbol{w}}^{\boldsymbol{T}}\boldsymbol{k}\bar{\boldsymbol{w}} \tag{18}$$

$$W_n=\frac{1}{2}\int_{-1}^{1}\left(\frac{2N(\xi,\ t)}{L}\right)\left(\sum_{i=1}^{N}\frac{\partial H_i(\xi)}{\partial\xi}\bar{w}_i(t)\right)^2 d\xi=\frac{1}{2}\bar{\boldsymbol{w}}^{\boldsymbol{T}}\boldsymbol{g}\bar{\boldsymbol{w}} \tag{19}$$

where, $\dot{\boldsymbol{w}}$ denotes the first derivative of $\boldsymbol{w}$ with respect to time. The matrices $\boldsymbol{m}$, $\boldsymbol{k}$ and $\boldsymbol{g}$ represent the mass matrix, stiffness matrix, and geometric stiffness matrix of the quadrature element, respectively. By employing numerical integration schemes (such as Gaussian or Gauss-Lobatto-Legendre (GLL) quadrature), the entries of these matrices can be expressed as follows:

$$m_{ij} = \int_{-1}^{1} \frac{m(\xi)L}{2} l_i(\xi) l_j(\xi)\, d\xi = \frac{L}{2}\sum_{k=1}^{N} G_k m(\xi_k)\, l_{ki}\, l_{kj} = \frac{L}{2} G_i m(\xi_i) l_{ij} \quad (i,j = 1,2,\dots,N) \tag{20}$$

$$g_{ij} = \frac{2}{L}\int_{-1}^{1} N(\xi,t)\frac{dH_i(\xi)}{d\xi}\frac{dH_j(\xi)}{d\xi} d\xi = \frac{2}{L}\sum_{k=1}^{N} N(\xi_k,t) G_k\, A_{ki} A_{kj} \quad (i,j = 1,2,\dots,N,N+1,N+2) \tag{21}$$

$$k_{ij} = \int_{-1}^{1}\left(\frac{8EI(\xi)}{L^3}\right)\frac{d^2H_i(\xi)}{d\xi^2}\frac{d^2H_j(\xi)}{d\xi^2} d\xi = \sum_{k=1}^{N} G_k \left(\frac{8EI(\xi_k)}{L^3}\right)\frac{d^2H_i(\xi_k)}{d\xi^2}\frac{d^2H_j(\xi_k)}{d\xi^2} d\xi$$
$$= \frac{8}{L^3}\sum_{k=1}^{N} G_k EI\,(\xi_k) B_{ki} B_{kj} \quad (i,j = 1,2,\dots,N,N+1,N+2) \tag{22}$$

Here, G_k denotes the weight corresponding to the integration point; A_{ij} and B_{ij} represent the weighting coefficients of the first and second derivatives of the shape function H_i at the element nodes, respectively. According to the differentiation rules of the DQM, these coefficients can be explicitly calculated.

$$\psi_j^{(k)}(\xi_i) = \frac{1}{(\xi_j - \xi_{N-j+1})}\begin{Bmatrix} l_j^{[k]}(\xi_i)(\xi_i - \xi_1)(\xi_i - \xi_N) + k(k-1) l_j^{[k-2]}(\xi_i) \\ + k l_j^{[k-1]}(\xi_i)[(\xi_i - \xi_1) + (\xi_i - \xi_N)] \end{Bmatrix} \quad (j = 1,N; i = 1,2,\dots,N) \tag{23}$$

$$\varphi_j^{(k)}(\xi_i) = \frac{1}{(\xi_j - \xi_{N-j+1})}\left[l_j^{[k]}(\xi_i)(\xi_i - \xi_{N-j+1}) + k l_j^{[k-1]}(\xi_i)\right] - \left[l'_j(\xi_j) + \frac{1}{\xi_j - \xi_{N-j+1}}\right]\psi_j^{[k]}(\xi_i) \quad (j = 1,N; i = 1,2,\dots,N) \tag{24}$$

$$\varphi_j^{(k)}(\xi_i) = \frac{1}{(\xi_j - \xi_1)(\xi_j - \xi_N)}\begin{Bmatrix} l_j^{[k]}(\xi_i)(\xi_i - \xi_1)(\xi_i - \xi_N) + k(k-1) l_j^{[k-2]}(\xi_i) \\ + k l_j^{[k-1]}(\xi_i)[(\xi_i - \xi_1) + (\xi_i - \xi_N)] \end{Bmatrix} \quad (j = 2,3,\dots,N-1; i = 1,2,\dots,N) \tag{25}$$

After obtaining A_{ij} by setting k=1, B_{ij} can be conveniently calculated using the following expression:

$$B_{ij} = \sum_{k=1}^{N} A_{ik} A_{kj} \tag{26}$$

2.2.2 Global governing equation

The global governing equation of the structure considering the P–Δ effect can be obtained by assembling the element matrices.

$$\boldsymbol{M}\ddot{\boldsymbol{w}} + (\boldsymbol{K} - \boldsymbol{G})\boldsymbol{w} = \boldsymbol{F} \tag{27}$$

where, $\boldsymbol{M}$ denotes the global mass matrix, $\boldsymbol{K}$ the global stiffness matrix, $\boldsymbol{G}$ the global geometric stiffness matrix, $\boldsymbol{F}$ the global equivalent load vector, and $\boldsymbol{w}$ the vector of lateral nodal displacements of the structure.

For a cantilever beam model discretized into Z elements with N nodes per element, the global equivalent load vector is denoted by $\boldsymbol{F} = \{\boldsymbol{F}_w^T, \boldsymbol{\Omega}_\theta^T\}^T$, namely

$$\boldsymbol{F}_w = \{f_1^{e1}, \dots, f_N^{e1} + f_1^{e2}, \dots, f_N^{e2} + f_1^{e3}, \dots, \dots, f_N^{eZ}\}^T \tag{28}$$

$$\boldsymbol{\Omega}_\Theta = \{\Omega_1^{e1}, \Omega_N^{e1} + \Omega_1^{e2}, \dots, \dots, \Omega_N^{eZ}\}^T \tag{29}$$

When constructing the global stiffness matrix of the structure using the QEM, the effects of nodal rotations are inherently included. However, the primary interest lies in the nodal transverse displacement response. To this end, the horizontal displacement vector $\boldsymbol{W}$ is designated as the primary degrees of freedom, while the nodal rotation vector $\boldsymbol{\theta}$ is treated as dependent degrees of freedom. Accordingly, the displacement and rotation components can be decoupled, and the structural vibration governing equation can be written as:

$$\begin{bmatrix} \boldsymbol{M}_w & \boldsymbol{0} \\ \boldsymbol{0} & \boldsymbol{M}_\theta \end{bmatrix}\begin{Bmatrix} \ddot{\boldsymbol{W}} \\ \ddot{\boldsymbol{\theta}} \end{Bmatrix} + \begin{bmatrix} \boldsymbol{K}_{ww} & \boldsymbol{K}_{w\theta} \\ \boldsymbol{K}_{\theta w} & \boldsymbol{K}_{\theta\theta} \end{bmatrix}\begin{Bmatrix} \boldsymbol{W} \\ \boldsymbol{\theta} \end{Bmatrix} = \begin{Bmatrix} \boldsymbol{F}_w \\ \boldsymbol{\Omega}_\theta \end{Bmatrix} \tag{30}$$

By setting $\boldsymbol{M}_\theta=\boldsymbol{0}$, the following is obtained:

$$\boldsymbol{\theta} = \boldsymbol{K}_{\theta\theta}^{-1}\boldsymbol{\Omega}_\theta - \boldsymbol{K}_{\theta\theta}^{-1}\boldsymbol{K}_{\theta w}\boldsymbol{W} \tag{31}$$

$$\boldsymbol{M}_w\ddot{\boldsymbol{W}} + \boldsymbol{K}_w\boldsymbol{W} = \boldsymbol{F} \tag{32}$$

Here

$$\boldsymbol{K}_w = \boldsymbol{K}_{ww} - \boldsymbol{K}_{w\theta}\boldsymbol{K}_{\theta\theta}^{-1}\boldsymbol{K}_{\theta w}$$

$$\boldsymbol{F} = \boldsymbol{F}_w - \boldsymbol{K}_{w\theta}\boldsymbol{K}_{\theta\theta}^{-1}\boldsymbol{W}_\theta$$

It is evident that Eq. (32) represents the standard structural dynamic governing equation, which involves only the primary degree of freedom vector $\boldsymbol{W}$. Once this governing equation is established, the dynamic response of the structure can be obtained using the unconditionally stable Newmark average acceleration method.

3. Verification and Method Comparison

3.1 Bridge Piers and Seismic Motions

Tubaldi [1,14] demonstrated that tall piers exhibit pronounced sensitivity in their dynamic characteristics to axial loading; However, his analytical model is not capable of addressing scenarios involving time-varying axial forces induced by significant vertical seismic components. Accordingly, this section employs one real tall bridge-pier, provided by Li [17], to conduct a bidirectional seismic response analysis using the proposed methods. The tall pier is characterized by a cracked-section stiffness of EI=2.225×108 kN·m², a distributed mass of $m(y)$=19.87 t/m, and a concentrated top mass of M_T=700 t. The corresponding mechanical models are illustrated in Fig. 3.

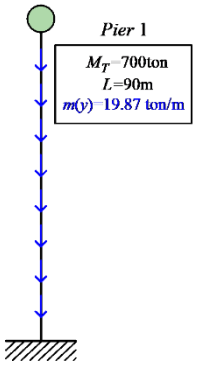

Fig. 3. Parameters of real bridge pier case.

This study utilizes the classical 1941 El Centro earthquake record, which includes vertical components. Fig. 4 depicts their acceleration time histories. Notably, when using the DQM, the continuous mass distribution function $m(y)$ must be interpolated to smoothly incorporate the concentrated top mass M_T. In contrast, within the QEM framework, M_T can be directly assigned to the last entry of the global mass matrix—namely, at the final node of the last element.

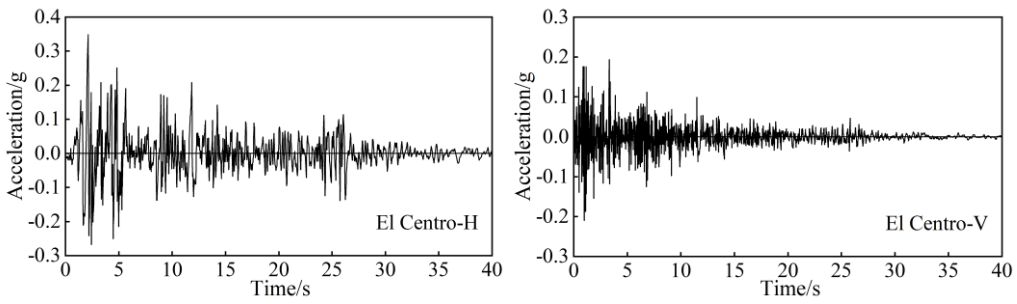

Fig. 4. Time history of horizontal and vertical seismic acceleration.

3.2 Comparison of Dynamic Characteristics

Table 1 provides a detailed comparison of the first three natural vibration periods of the pier under both unloaded and axially loaded conditions, as calculated using the DQM, the QEM, and the analytical solution proposed by Tubaldi [14]. These comprehensive results offer a clear basis for evaluating the accuracy and reliability of the numerical methods in relation to the analytical benchmark.

Table 1. The first three order natural periods for pier 1(s).

Mode	Without axial load			With axial load		
	DQM	Tubaldi	QEM	DQM	Tubaldi	QEM
1	6.9445	6.968	6.9681	7.6619	7.692	7.6919
2	0.8781	0.884	0.8840	0.8891	0.895	0.8950
3	0.2899	0.292	0.2919	0.2912	0.293	0.2932

The above table illustrate the influence of axial loads on the structural characteristics of bridge piers. Building upon this, the QEM introduced in this study can be further employed to investigate the effects of time-varying axial forces on structural characteristics in greater depth. This influence is further illustrated by the structural configuration shown in the figure below.

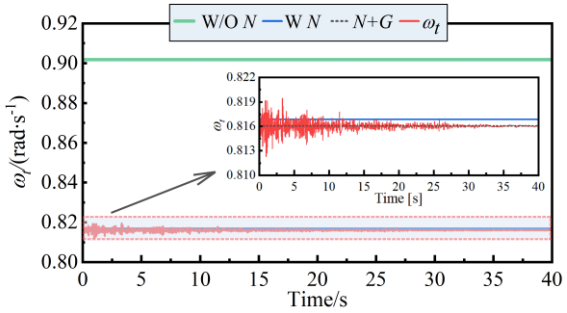

Fig.5. Structural natural frequency under different loading states.

In Fig. 5, N denotes the vertical axial force, G represents the vertical seismic load, and ω_t indicates the time-varying frequency. Under the influence of time-dependent axial loading, the structural frequency is no longer constant but varies with changes in axial force. As shown in the figure, after accounting for the P–Δ effect, the fundamental frequency of the structure decreases from 0.9016 to 0.8168. Furthermore, when the time-varying axial force is considered, the structural frequency exhibits a slight additional reduction (approximately 0.09%). Subsequently, the time history of the structural frequency closely follows the profile of the vertical ground motion. This phenomenon arises from the assumption of infinite axial stiffness, which neglects axial deformation and directly equates the vertical load to the axial force.

3.3 Comparison of seismic response

The top of the pier was chosen as the observation point to compare and analyze the time-history responses under P-Δ effects and time-varying axial forces (vertical seismic motion), and to examine its maximum lateral displacement characteristics.

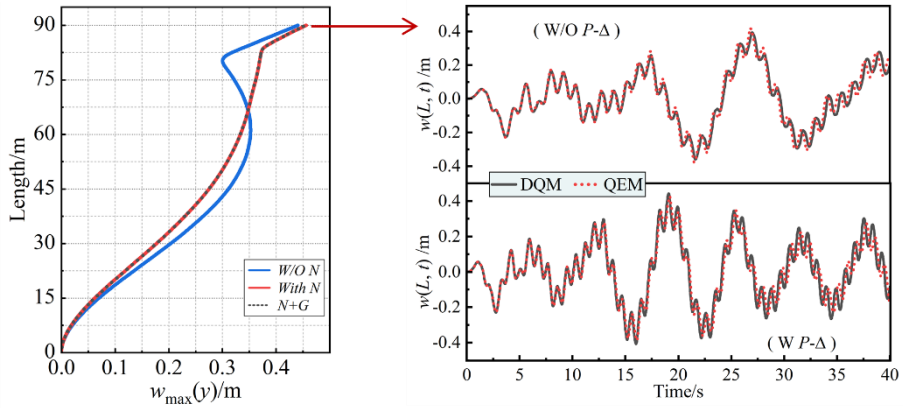

Fig.6. Maximum lateral displacement and time histories curve at the pier top.

It can be observed that the results obtained from DQM and QEM are largely consistent, which verifies the accuracy and feasibility of both numerical methods in structural dynamic analysis. In addition, the results considering the second-order gravity effect are nearly identical to those that also account for time-varying axial forces. This is because, although time-varying axial forces can alter the natural frequency of the structure, the magnitude of this influence is relatively small, and thus their overall impact on structural response is limited.

4. Conclusions

Two high-precision methods for dynamic *P*–Δ analysis of bridge piers are discussed. Compared with conventional approaches, these methods not only accommodate static axial loads but also effectively handle responses under coupled bidirectional seismic excitations. Crucially, both achieve high-accuracy solutions without complex iterative procedures. The main conclusions are:

(1) The *P*–Δ effect can be either beneficial or detrimental, depending on the magnitude of external loads and the relationship between the pier's natural frequencies and the excitation frequencies.

(2) The high-precision *P*–Δ analysis based on the Quadrature Element Method (QEM) shows greater adaptability in dealing with geometric or material discontinuities. Compared to the Differential Quadrature Method (DQM), QEM is more convenient and flexible for practical applications.

(3) Neglecting axial deformation, the influence of time-varying axial forces on bridge piers is relatively minor, since their effect on the geometric stiffness matrix is limited. Consequently, the structure's natural frequencies do not undergo significant fluctuations, and this influence can be considered negligible.

Declaration of Competing Interest

The authors declare that they have no known competing financial interests or personal relationships that could have appeared to influence the work reported in this paper.

Acknowledgments

This work was financially supported by the National Natural Science Foundation of China under Grant No. 52378519.

References:

[1] E. Tubaldi, F. Scozzese and D.D. Domenico, Effects of axial loads and higher order modes on the seismic response of tall bridge piers, Eng. Struct. 247 (2021) 113-134.

[2] Kolias B. Overview of seismic issues for bridge design. In Athanasopoulou A, Poljansek M, Pinto A, Tsionis G, Denton S eds. Workshop “Bridge Design to Eurocodes 2010; Vienna, Austria.
[3] Mitoulis S.A. (2012). “The inefficacy of seismic isolation in bridges with tall piers”, In Proc., 15th WCEE - World Conference on Earthquake Engineering, Lisbon, Portugal, paper No 3944.
[4] Mitoulis S.A. “Bridges with fixities and bearings vs isolated systems”, COMPDYN 4th International Conference in Computational Methods in Structural Dynamics and Earthquake Engineering, Kos, Greece, 12-14 June 2013.
[5] European Committee for Standardization (ECS). Eurocode 8: Design of structures for earthquake resistance. European Committee for Standardization. Brussels, Belgium, 2005.
[6] AASHTO. LRFD bridge design specifications, 6th edition. Washington, DC; 2012.
[7] Specifications for Seismic Design of Highway Bridges, JTG/T 2231-01—2020. Beijing, 2020.
[8] Chen Xu, Li Chunxiang. Seismic performance of tall pier bridges retrofitted with lead rubber bearings and rocking foundation. Eng Struct 2020; 212: 110529.
[9] Chen Xu, Xiang Nailiang, Li Chunxiang. Influence of higher-order modes of slender tall pier bridge columns on the seismic performance of pile foundations. Soil Dyn Earthquake Eng 2021; 142: 106543.
[10] Chen Xu, Guan Zhongguo, Spencer Billie F, Li Jianzhong. A simplified procedure for estimating nonlinear seismic demand of tall piers. Eng Struct 2018; 174: 778–91.
[11] Chen Xu, Guan Zhongguo, Li Jianzhong, Spencer Billie F. Shake table tests of tall-pier bridges to evaluate seismic performance. J Bridge Eng 2018; 23(9): 04018058.
[12] Mei Zhu, Wu Bin, Bursi Oreste S, Xu Guoshan, Wang Zhen, Wang Tao, et al. Hybrid simulation with online model updating: Application to a reinforced concrete bridge endowed with tall piers. Mech Syst Sig Process 2019; 123: 533–53.
[13] Liu Yang, Mei Zhu, Wu Bin, Bursi Oreste S, Dai Kao-shan, Li Bo, et al. Seismic behaviour and failure-mode-prediction method of a reinforced-concrete rigid-frame bridge with thin-walled tall piers: Investigation by model-updating hybrid test. Eng Struct 2020; 208: 110302.
[14] Tubaldi E, Tassotti L, Dall’Asta A, Dezi L. Seismic response analysis of slender bridge piers. Earthquake Eng Struct Dyn 2014;43(10):1503–19.
[15] Lu Y, Zhai Y, Li H, et al. P–Δ Effect Analysis of Tall Slender Structures Subjected to Arbitrary Time-Variant Axial Forces: A Differential Quadrature-Based Approach[J]. International Journal of Structural Stability and Dynamics, 2025: 2650178.
[16] Wang, X W. Differential quadrature and differential quadrature based element methods: theory and applications[M]. Butterworth-Heinemann, Oxford, 2015.
[17] J. Z. Li, Z. Y. Liang and C. Y. Jiao, Investigation on rational analytical model of tall bridge pier, Proceedings of the 14th World Conference on Earthquake Engineering 2008; October 12-17, 2008, Beijing, China.
[18] B. Kolias, Overview of seismic issues for bridge design, In Athanasopoulou A, Poljansek M, Pinto A, Tsionis G, Denton S eds. Workshop Bridge Design to Eurocodes 2010, Vienna, Austria.